ACS APPLIED MATERIALS & INTERFACES

Research Article

www.acsami.org

Controlling $CH_3NH_3PbI_{3-x}Cl_x$ Film Morphology with Two-Step Annealing Method for Efficient Hybrid Perovskite Solar Cells

Dong Liu,[†] Lili Wu,*[,†] Chunxiu Li,[†] Shengqiang Ren,[†] Jingquan Zhang,*[,†] Wei Li,[†] and Lianghuan Feng[†]

[†]Institute of Solar Energy Materials and Devices, College of Materials Science and Engineering, Sichuan University, No. 24 South Section 1, Yihuan Road, Chengdu, China, 610064

Supporting Information

ABSTRACT: The methylammonium lead halide perovskite solar cells have become very attractive because they can be prepared with low-cost solution-processable technology and their power conversion efficiency have been increasing from 3.9% to 20% in recent years. However, the high performance of perovskite photovoltaic devices are dependent on the complicated process to prepare compact perovskite films with large grain size. Herein, a new method is developed to achieve excellent $CH_3NH_3PbI_{3-x}Cl_x$ film with fine morphology and crystallization based on one step deposition and two-step annealing process. This method include the spin coating deposition of the perovskite films with the precursor solution of PbI_2, $PbCl_2$, and CH_3NH_3I at the molar ratio 1:1:4 in dimethylformamide (DMF) and the post two-step annealing (TSA). The first annealing is achieved by solvent-induced process in DMF to promote migration and interdiffusion of the solvent-assisted precursor ions and molecules and realize large size grain growth. The second annealing is conducted by thermal-induced process to further improve morphology and crystallization of films. The compact perovskite films are successfully prepared with grain size up to 1.1 μm according to SEM observation. The PL decay lifetime, and the optic energy gap for the film with two-step annealing are 460 ns and 1.575 eV, respectively, while they are 307 and 327 ns and 1.577 and 1.582 eV for the films annealed in one-step thermal and one-step solvent process. On the basis of the TSA process, the photovoltaic devices exhibit the best efficiency of 14% under AM 1.5G irradiation (100 mW·cm^{-2}).

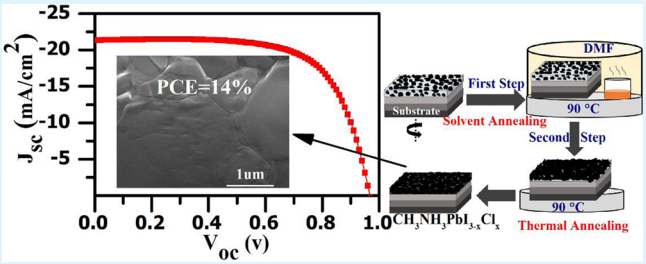

KEYWORDS: *perovskite solar cells, morphology, two-step annealing, crystallinity, grain size*

1. INTRODUCTION

Organic/inorganic hybrid photovoltaic materials and devices have recently attracted a great deal of attention because they exhibit functionality, high molar extinction coefficient, structure regulation, low cost of the organic component, high carrier transporting properties and high stability of the inorganic materials.[1−4] In the past few years, perovskite thin film photovoltaic devices are rapidly development for their excellent photovoltaic performance.[3,5,6] Recent progress with PCE over 20% in perovskite planar heterojunction cells has been demonstrated by chemical composition engineering.[7] They have shown great promise for cost competitive solar power via reduced material fabrication costs as compared with traditional thin film photovoltaic devices (e.g., CdTe solar cells),[8] which are the new members in the field of the third-generation photovoltaics technology.

For typical fabrication of planar heterojunction perovskite solar cells, perovskite thin films are prepared via solution-processed deposition method and vacuum vapor deposition.[9,10] Thermal deposition requires high vacuum, which increases the manufacturing costs. So the solution-processed deposition process is widely adopted. During the perovskite polycrystalline films preparation process, because of the reaction PbI_2 or $PbCl_2$ with CH_3NH_3I with rapid evaporation of solvent, the perovskite polycrystalline films are fast nucleation, growth, and further crystallization.[11] One issue with solution-processed perovskite films is that changing process conditions to control the crystallization behavior and ensure high film morphology quality. However, several factors such as precursor concentration, spin conditions and annealing process can easily affect the film morphological evolution.[12−14] To realize high performance of perovskite solar cells, reducing the pinhole defects, increasing compactness and controlling crystallinity still remain a challenging issue.[14−17] Previous studies of improving morphology quality and crystallinity include vacuum-assisted thermal annealing method,[18] two-step thermal annealing method,[19] CH_3NH_3Cl-assisted crystallization,[20] low-pressure vapor annealing process,[21] adding additive enhanced crystallization,[22−24] low-temperature gas−solid crystallization process,[25] solution chemistry engineering,[16] etc. Although these results show improvements of morphology and photovoltaic performance as well, it is difficult to effectively achieve high quality large grain size perovskite films by the conventional solution approaches. However, high quality controlled perov-

Received: April 17, 2015
Accepted: July 8, 2015
Published: July 8, 2015

DOI: 10.1021/acsami.5b03324
ACS Appl. Mater. Interfaces 2015, 7, 16330−16337

Scheme 1. Schematic of the Two-Step Solvent-Assisted Annealing Process of Fabricated $CH_3NH_3PbI_{3-x}Cl_x$ Film

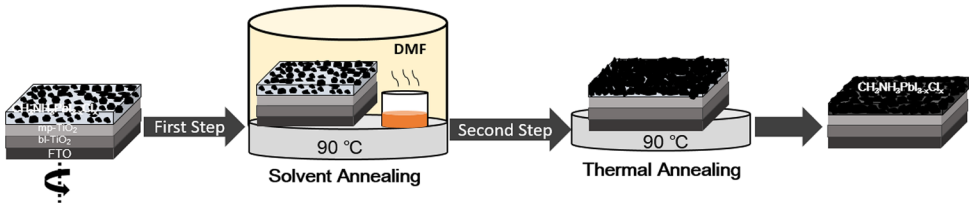

skite films often require complicated process conditions, such as antisolvent vapor-assisted crystallization approach,[26] hot-casting techniques.[27] Therefore, developing a simple and effective method for regulating the morphology and crystallization of perovskite films is highly demanded.

In this work, the two-step annealing (TSA) method was proposed for controlling morphology and grain growth process of the perovskite film for the first time. The $CH_3NH_3PbI_{3-x}Cl_x$ film preparing process involved one step deposition through optimizing the ratio of perovskite precursor solution and two-step annealing process, which could effectively increase the crystallinity and improve morphology quality. The films prepared based on TSA process were characterized by the scanning electron microscope (SEM), the X-ray diffraction (XRD) and the transmittance spectra, in comparison with the films via one-step solvent annealing (OSA) and one-step thermal annealing (OTA) processes. Then the photovoltaic devices were prepared and the dependence of their performance were discussed in the various process conditions. The fabricated photovoltaic devices based two-step annealing process exhibited the best PCE up to 14% under AM 1.5G irradiation (100 mW.cm^{-2}).

2. EXPERIMENTAL SECTION

2.1. Materials. PbI_2, titanium diisopropoxide bis(acetylacetonate) (75% in isopropanol) and dimethylformide (DMF) were purchased from Alfar Aesar. $PbCl_2$ was purchased from Aldrich. 2,2′,7,7′-Tetrakis[N,N-di(4-methoxyphenyl)amino]-9,9′-spirobifluorene (spiro-MeOTAD) was purchased from Luminescence Technology Corp. All of the reagents were used without further purification. CH_3NH_3I was synthesized by the method reported in the literature.[28] Substrates were fluorine-doped tin oxide conducting glass (FTO, Pilkington, thickness: 2.2 mm, sheet resistance 14Ω/square).

2.2. Device Fabrication. The device structure was FTO/bl-TiO_2/mp-TiO_2/$CH_3NH_3PbI_{3-x}Cl_x$/spiro-MeOTAD/Au. The FTO substrate was cleaned first with detergent, and then sequentially rinsed with deionized water, acetone and ethanol, finally dried with N_2.

The compact TiO_2 of 50 nm as hole blocking layer (bl-TiO_2) and the mesoporous TiO_2 layer (mp-TiO_2) of 300 nm were deposited on the FTO substrate. The bl-TiO_2 layer was first prepared through spray pyrolysis of titanium diisopropoxide bis(acetylacetonate) (75% in isopropanol) diluted in anhydrous ethanol at a volumetric ratio of 1:40 using N_2 as a carrier gas on a preheated hot plate at 350 °C. And second the as-deposited bl-TiO_2 film was transferred to annealing furnace and annealed in air at 500 °C for 30 min. The mp-TiO_2 layer was first spin-coated on the surface of the bl-TiO_2 layer at 4000 rpm for 40 s using TiO_2 paste (Dyesol 18NR-T) diluted in anhydrous ethanol at 2:7 by weight, which was heated at 130 °C for 5 min After it was cooled to room temperature, the mp-TiO_2 layer was transferred to annealing furnace and annealed in air at 500 °C for 60 min.

The $CH_3NH_3PbI_{3-x}Cl_x$ films were formed with one step spin coating procedure by the hybrid solution. The CH_3NH_3I was mixed with PbI_2 and $PbCl_2$. The mole ratio of PbI_2/$PbCl_2$/CH_3NH_3I was 1:1:4 in anhydrous DMF, shaking at room temperature for 2 h to produce clear perovskite precursor solution with concentration of 40 wt %. The perovskite precursor solution was filtered with a PTFE filter with 0.45 μm pore size to obtain more transparent precursor solution.

To deposit perovskite films, the perovskite precursor solution was transferred to N_2 glovebox with moisture content less than 50 ppm, then heated and stirred at 70 °C. The perovskite precursor solution was dropped onto the TiO_2-coated FTO substrate. The substrate was then spun at 4000 rpm for 30s. The obtained perovskite film was then dried at 90 °C for about 2 min. The color changed from transparent to light brown.

The as-deposited perovskite films were heat treated with OTA, OSA, and TSA process, respectively. For the OTA process, the deposited perovskite film was continued thermal annealing at 90 °C for 60 min. For the OSA process, the perovskite film and a smaller glass vial on the hot plate was covered by a glass vials. A smaller glass vial was filled with 100 uL DMF solvent nearby the perovskite film. DMF solvent could promote the perovskite film morphology coverage and crystalline performance enhancement. The perovskite film was kept solvent annealing condition at 90 °C for 30 min. For the TSA process the perovskite film heat treated through OSA process was continued annealing under thermal condition at 90 °C for 45 min in glovebox with relative humidity below 5%. The final perovskite film was brown-black.

The hole transport layer was spin-coated on the surface of perovskite layer at 2000 rpm for 30 s by mixture solution of Spiro-MeOTAD dissolved in chlorobenzene (72 mg/1 mL), 17 μL of Li-bis(trifluoromethanesulfonyl)-imide (Li-TFSI) dissolved in acetronitrile (520 mg/mL) and 20 μL of *tert*-butylpyridine (t-BP). Finally devices were left in the dark in air overnight prior to thermal evaporation of ∼100 nm Au electrodes to complete the solar cells.

2.3. Characterizations. X-ray diffraction measurements was performed using a DX-2600 X-ray diffractometer (Dandong Fangyuan Instrument Company, China) with Cu Ka radiation and the scan range from 10° to 70°.The transmittance spectra of perovskite films on the TiO_2 substrate were recorded using a PerkinElmer Lambda 950 UV−vis Spectrometer. A field emission scanning electron microscope (Hitachi S-4300) was used to acquire SEM images. Time-resolved photoluminescence spectra were obtained using an Edinburgh Instruments FLS 980 fluorescence spectrometer. The perovskite films being used as PL measurements were covered with a poly(methyl methacrylate) (PMMA) layer to prevent degradation by ambient moisture.

The current−voltage characteristics were measured (2400 SourceMeter, Keithley Instruments) under simulated AM 1.5 G sunlight at 100 mW·cm^{-2} irradiation generated using an AAB ABET technologies Sun 2000 solar simulator and calibrated using an GaAs reference cell to trace NREL standard. One metal mask was used to define the Au layer area in the vacuum deposition process and the perovskite films beyond the Au were removed in order to minimize any edge effects. The Au layer area is 0.07 cm^2 for most solar cell and the area is 0.18 cm^2 for the samples used as EQE measurements.

The external quantum efficiency (EQE) was measured using a QEX10 solar cell quantum efficiency measurement system (PV Measurements, Inc.), and was calibrated with a Si diode sourced to NIST before measurement. Agilent 4294A was used to acquire impedance spectroscopy data with the frequency range of 40 Hz−100 kHz under dark condition.

DOI: 10.1021/acsami.5b03324
ACS Appl. Mater. Interfaces 2015, 7, 16330−16337

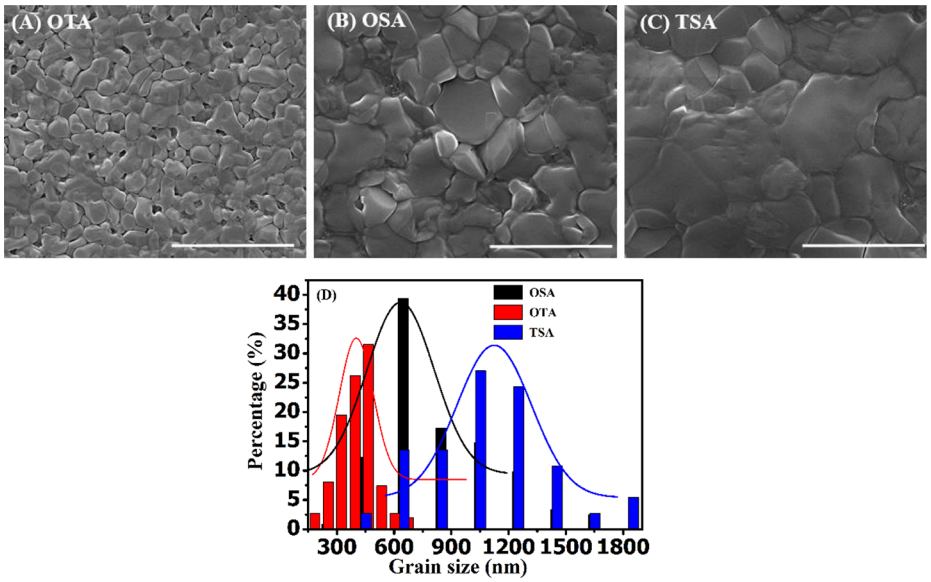

Figure 1. SEM images of the one-step thermal annealing (A), one-step solvent annealing (B), and two-step annealing (C) of $CH_3NH_3PbI_{3-x}Cl_x$ perovskite film (the scale bars in the SEM micrographs are 3 μm). (D) Grain size distributions of the perovskite films corresponding to SEM images.

3. RESULTS AND DISCUSSION

The $CH_3NH_3PbI_{3-x}Cl_x$ perovskite films were fabricated by the one step deposition, two-step solvent-assisted annealing process, as illustrated in Scheme 1. The morphological features and crystallization of the films are dependent on the composition of the precursor solution and the thermal history in the whole TSA process.

For the perovskite film preparing method, the mole ratio of PbI_2: $PbCl_2$: CH_3NH_3I was optimized as 1:1:4 for the dimethylformamide (DMF) precursor solution. Our previous studies showed that the films morphology was dendritic with low surface coverage when the mole ratio of PbI_2 and CH_3NH_3I was 1:1 (Supporting Information Figure S1), which is consistent with literatures.[11,16] However, compared with the PbI_2-based method, it was obviously improved when introducing $PbCl_2$. which significantly enhanced film surface coverage and uniformity.[29] The reaction kinetics of the perovskite formation were showed in step 1−3

$$PbI_2 + CH_3NH_3ICH_3NH_3PbI_3 \quad (1)$$

$$PbCl_2 + 3CH_3NH_3ICH_3NH_3PbI_{3-x}Cl_x + (2 - x)HCl + 2CH_3NH_2 + xHI \quad (2)$$

$$CH_3NH_3PbI_3 + PbCl_2 + 3CH_3NH_3I2CH_3NH_3PbI_{3-x}Cl_x + (2 - 2x)HCl + 2CH_3NH_2 + 2xHI \quad (3)$$

In the reaction process, CH_3NH_3Cl intermediate is formed, which delays the formation time of $CH_3NH_3PbI_{3-x}Cl_x$ perovskite.[18] It is beneficial to perovskite crystallization process.[20] After spin-coating the $CH_3NH_3PbI_{3-x}Cl_x$ perovskite film, the color of the as-deposited film was slowly changed from transparent to light brown in a few minutes. It became dark gradually when the film substrate was solvent-induced annealed at 90 °C in DMF vapor. Solvent vapor environment promote the precursor ions and molecules diffusing a longer distance, which can increase the perovskite grain size and film uniformity.[30] However, the vaporization of the formed $CH_3NH_3PbI_{3-x}Cl_x$ perovskite films could be accelerated in the DMF vapor environment, which could deteriorate the morphology and surface coverage of the film. So the thermal annealing process without DMF is adopted to further improve the crystallinity and morphology quality as illustrated in Scheme 1. The surface coverage is significantly improved in the thermal annealing condition.

Figure 1 shows the scanning electron microscopy (SEM) images of $CH_3NH_3PbI_{3-x}Cl_x$ perovskite films at different annealing conditions and grain size distributions corresponding to SEM images. The thermal annealed perovskite film shows relatively small in-plane grain size. The average grain size is about 400 nm, while the grain boundary cracks formation associate with multiple orientation grains. The morphological features are different from others as illustrated in Figure 1A. Pore structure of the perovskite for accumulation were observed. Such pinhole defects possibly derive from generating and releasing of byproducts via reaction 3, for example, CH_3NH_3, HCl vapor.[18] In the following case, the perovskite films are treated with solvent annealing. Compared with thermal annealing, the grain growth size increase to approximately 700 nm as shown in Figure 1B. We observe most of grain boundary cracks decrease. The precursor ions and molecules promote migration and interdiffusion via the solvent-assisted processing, which leads to sustainable growth and crystallization of perovskite film in relatively short time. Only a few pores are formed in the morphological features. To achieving better perovskite film, two-step annealing process is developed. Figure 1C shows that this annealing method can form nearly continuous, compact perovskite film based on this annealing process. We choose lower temperature, long time annealing method to realize perovskite large grain growth. The grain growth size become larger, increasing to approximately 1.1 μm, which shows significantly increase in grain size for conventional thermal annealing method. It is noted that the grain size of the second annealed films grows with increased annealing time. The rate of grain growth is saturated in the 45 min. Surface channeling crack features will appear with further annealing in perovskite film systems (Supporting Information Figure S2).

DOI: 10.1021/acsami.5b03324
ACS Appl. Mater. Interfaces 2015, 7, 16330−16337

The annealing-induced crystallinity changes were measured by X-ray diffraction (XRD). Figure 2 displays the XRD spectra

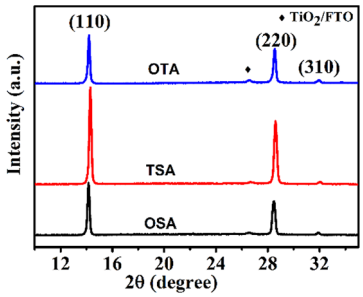

Figure 2. XRD patterns of the perovskite films on TiO_2 substrate fabricated with different annealing methods as labeled shown.

of perovskite films fabricated with different annealing methods. The main diffraction peaks in the XRD spectra at 14.2°, 28.5°, and 32° are assigned to the 110, 220, and 310 peaks, respectively. It indicates that the polycrystalline $CH_3NH_3PbI_{3-x}Cl_x$ film are the orthorhombic crystal structure.[17] The perovskite film with two-step annealing shows strong XRD peaks with high preferred orientation, which reveals that the strategies are effective for controlling crystallization of high quality perovskite film.

Figure 3 show the transmittance spectra and absorption coefficient of the perovskite films with different annealing treatments. As can be seen in Figure 3, the transmittance of the film with two-step annealing treatments is lower than that of thermal annealing and solvent annealing film treatments. The band-edge absorption of all perovskite films shows onset at around 800 nm (corresponding to 1.55 eV for absorption coefficient) with a broad absorption in the visible region. Based on the absorption coefficient, the optical band gaps (E_g) were calculated from the eq 1 by assuming a direct transition:

$$(\alpha h\nu)^2 = A(h\nu - E_g) \quad (1)$$

where A, h, and α represent constant, Planck constant, absorption coefficient, respectively. For the solvent annealed, thermal annealed and two-step annealed samples, E_g can be estimated to be 1.582, 1.577, and 1.575 eV, respectively. The optical band gaps are close to the report elsewhere.[29] The optical band gaps show slight red shift with two-step annealing methods, which should be due to the improved crystallinity and lattice orientation with this condition. It exhibits high absorption of light and light harvesting capacity as shown in Figure 3b.

To investigate the effect of different morphological features of $CH_3NH_3PbI_{3-x}Cl_x$ films with different annealing treatments on recombination. We measured steady-state photoluminescence spectra (Figure 4a) and time-resolved photoluminescence spectra (Figure 4b) based on time-correlated single photon counting (TCSPC). The peak emission of the PL spectra at 772 nm was observed, which was consistent with previous reports.[31] Figure 4b shows the time-resolved photoluminescence of $CH_3NH_3PbI_{3-x}Cl_x$ film on glass substrate with different annealing methods. The lifetime were fitted with three exponential decay curves (here, the longer lifetime was used for comparison).[32] Extremely the $CH_3NH_3PbI_{3-x}Cl_x$ film shows long lifetime of 327 ns, which is comparable to the value found in $CH_3NH_3PbI_{3-x}Cl_x$ film in previous reports.[31] It is probably derived from the Cl anions doping roles in perovskite film.[32] The PL decay lifetime of the sample with two-step annealing is 460 ns, which is longer than that of the samples with solvent (307 ns) and thermal annealing (327 ns). It indicates the improved crystallinity suppresses the nonradiative recombination channels.

Photovoltaic devices were fabricated to evaluate the influence of improved crystallinity and morphology on device performance. FTO/bl-TiO_2/mp-TiO_2/$CH_3NH_3PbI_{3-x}Cl_x$/spiro-MeO-TAD/Au perovskite devices were fabricated. Figure 5 provide typical current−voltage characteristics and external quantum efficiency (EQE) of the devices derived from different annealing processes. Table 1 shows relevant average photovoltaic parameters corresponding to perovskite layers. Photovoltaic performances of these perovskite devices were measured under AM 1.5 G, 100 mW cm^{-2} light illumination. Devices with the two-step annealed $CH_3NH_3PbI_{3-x}Cl_x$ perovskite layer deliver short-circuit current (J_{sc}) of 19.19 mA/cm^2, open circuit voltage (V_{oc}) of 1.0 V, fill factor (FF) of 67%, corresponding to PCE of 12.88%, which are significantly higher than that of thermal annealing (J_{sc} of 16.56 mA/cm^2, V_{oc} of 1.0 V, FF of 57.89%) and solvent annealing (J_{sc} of 12.83 mA/cm^2, V_{oc} of 0.88 V, FF of 68.5%) treatments. Compared with thermal annealed and solvent annealed devices, the obtained improvement of PCE results from better perovskite film crystallinity and morphology coverage. A best PCE of 14.05% was obtained with J_{sc} of 21.35 mA/cm^2, V_{oc} of 0.97 V and FF of 68%. Long-time solvent annealed devices were also tested, as shown in Figure S3 in the Supporting Information. PCE of 10.17% was obtained, which showed slightly higher than that of thermal annealed devices. Because of high light harvesting capacity with higher surface coverage,[25] majority of photons are collected to generating photo current. The increased crystallinity with fewer defects decreases grain boundary density. Most of the photogenerated charges can reach the

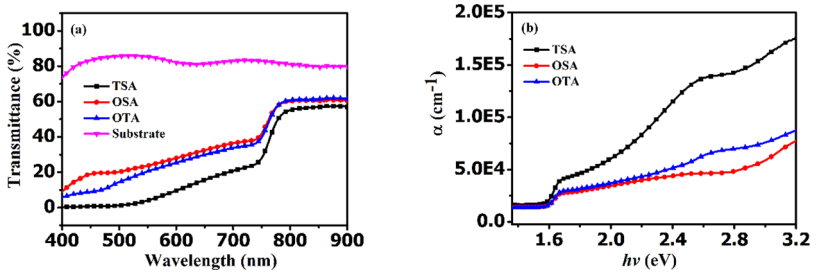

Figure 3. (a) Transmittance spectra and (b) absorption coefficient of the perovskite films coated TiO_2 substrate depending on different annealing methods as labeled shown.

DOI: 10.1021/acsami.5b03324
ACS Appl. Mater. Interfaces 2015, 7, 16330−16337

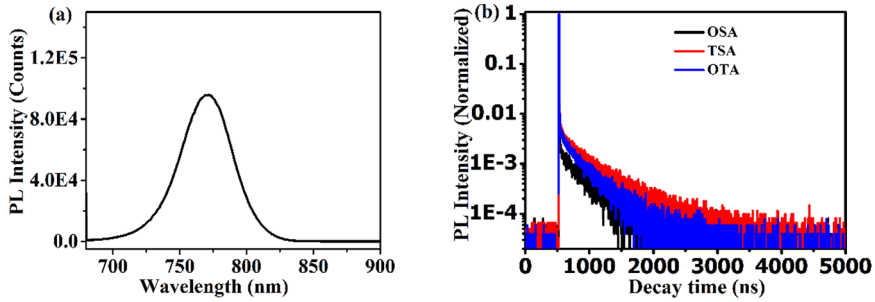

Figure 4. (a) Photoluminescence spectra of $CH_3NH_3PbI_{3-x}Cl_x$ film coated on glass substrate. (b) Time-resolved photoluminescence of $CH_3NH_3PbI_{3-x}Cl_x$ films taken at the peak emission of 772 nm depending on different annealing methods as labeled shown.

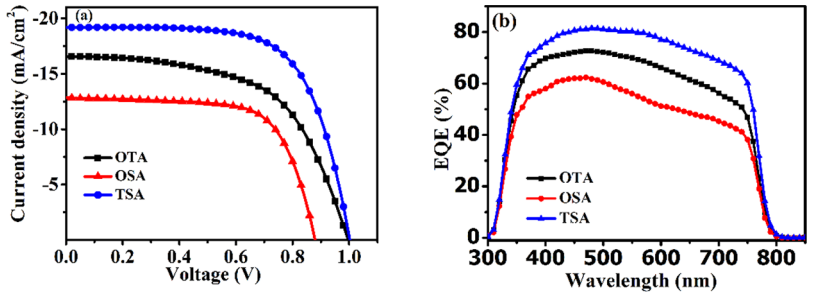

Figure 5. (a) Typical photocurrent density−voltage characteristics of the perovskite devices with different annealing methods measured under AM1.5 simulated sun light; (b) EQE spectra of the devices with different annealing methods.

Table 1. Detailed Photovoltaic Parameters of the Devices with Different Annealing Conditions Corresponding to Perovskite Layers[a]

annealing parameters	J_{sc} (mA/cm^2) (average)	V_{oc} (V) (average)	FF (%) (average)	PCE (%) (average)
OSA	13.06	0.86	65.24	7.35
OTA	15.0	0.97	61.1	8.95
TSA	18.87	0.99	66.63	12.4

[a]Based on 15 devices of each category.

electrodes via single grain, which can significantly reduce the charge recombination loss at grain boundaries in perovskite devices.[30] Additionally, the increased surface coverage can reduce the contact behavior between the TiO_2 substrate and Au electrode layer. In the case, shunting and leakage currents path should be inhibited, which reflects the increasing of FF and V_{oc} for photovoltaic devices performance.[33] As can be seen in the EQE response of the devices with different annealing methods, the devices show efficient charge extraction from 350 to 800 nm. It is consistent with the transmittance spectra of the perovskite films. The devices derived from solvent annealing

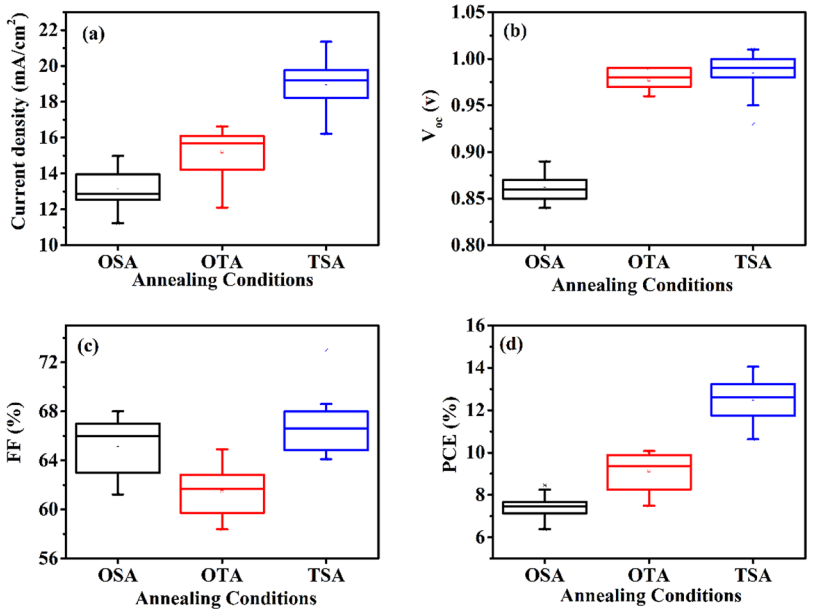

Figure 6. Box chart of photovoltaic parameters comparison with different annealing conditions.

DOI: 10.1021/acsami.5b03324
ACS Appl. Mater. Interfaces 2015, 7, 16330−16337

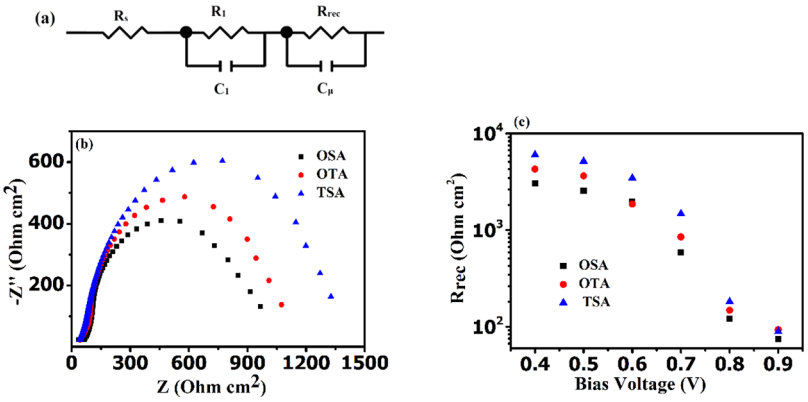

Figure 7. (a) Equivalent circuit employed to Nyquist fitting. (b) Impedance spectroscopy of the devices treated with different annealing conditions under dark conditions. (c) Recombination resistance (R_{rec}) at various bias voltages.

have slightly lower photocurrent than others because of insufficient crystallinity and absorption of the perovskite film from 520 to 800 nm. For two-step annealing treated perovskite films, due to large grain size and few grain boundaries and longer charge diffusion length, the photogenerated carriers can be effectively extracted out and transportation via single grain, decreasing charge recombination paths. In this case, the photocurrent of the two-step annealed devices show effectively increased EQE in the red spectrum region than the thermal annealed devices.

Figure 6a–d show the effects of photovoltaic parameters comparison with different annealing conditions. As can be seen in Figure 6a–d, the photovoltaic parameters values are significantly dependent on annealing conditions. J_{sc} and PCE of two-step annealed devices are higher than others. As previously mentioned, which is result from improvements of crystallinity and morphology. However, the solvent annealed devices have lower photocurrent density and PCE, probably as a result of incomplete crystallization during phase of forming organometal mixed halide, exhibiting cell shunting and poor light absorption.[33] Similarly, lower V_{oc} is obtained possibly resulting from increased charge recombination.[11] It is noticed that the thermal annealed devices show relatively lower FF (Figure 6c). This is probably due to the increased number of grain boundaries during annealing process, which lead to increase the series resistance (R_s) and decrease the fill factor.[28] According to the diode equivalent circuit model equation (eq2), where I_{ph}, I_0, q, V, n, k, and T represent photocurrent, reverse saturation current, electric charge, bias potential, fitting parameters (for perovskite photovoltaic devices, $n = 1$), Boltzmann constant, absolute temperature, respectively. R_s of the different annealed devices are estimated from the typical I–V curves.

$$I = I_{ph} - I_0\left\{\exp\left[\frac{q(V + IR_s)}{nkT}\right] - 1\right\} \quad (2)$$

For the solvent annealed, thermal annealed and two-step annealed devices, R_s is estimated to be 0.115, 0.21, and 0.11 Ω, respectively. As mentioned above, relatively high series resistance is ascribed to grain boundary crack formation. The solvent-assisted annealed devices show large size grain with low series resistance, probably as a result of fewer grain boundaries, which correlate with the observed high fill factor than that of thermal annealed devices. Hysteresis behavior in current–voltage curves are widely observed in perovskite solar cells with changed scanning conditions. The device shows hysteresis in the current–voltage curves (Supporting Information Figure S4) which is similar to the reports,[28] whereas V_{oc} remains almost unchanged and J_{sc} is lower at forward scanning as shown in Figure S4 because of the influence of the crystal size and the mesoporous TiO_2 layer.[34] Additionally, DMF vapor diffusing can effectively weaken the hysteresis behavior of the perovskite devices.[35] It is notable that the devices maintain more than 85% of its initial PCE after several months stored in nitrogen atmosphere. Open voltage and photocurrent show slightly decay, decreasing 2.1% and 1.6%, respectively. This indicates that the perovskite devices show promising long-term stability.

Impedance spectroscopy is used to investigate the internal charge carrier transportation and recombination for the devices.[36] Figure 7a–c show that the equivalent circuit model for fitting and impedance spectroscopy of the devices. R_s and R_{rec} are the series resistance and recombination resistance of the devices. In the Nyquist plots, Figure 7b shows the main arcs at high-frequency region and lower-frequency region, which is caused by $TiO_2/CH_3NH_3PbI_{3-x}Cl_x$/spiro-OMeTAD interface. The obtained R_s for fitting results of the devices for two-step annealing conditions is 2.9 Ω cm^2, which is lower than that of the one-step solvent (3.08 Ω cm^2) and thermal (3.4 Ω cm^2) annealing conditions. The results are agreement with the FF changes. It indicates that two-step annealing condition can promote internal charge carrier transportation and decrease charge loss process. The bias voltage dependence of R_{rec} for devices is shown in Figure 7c. The R_{rec} exponential decrease with voltage, which is similar to other reports.[20] The R_{rec} values for the devices with one-step annealing treatment are lower than that of the devices with two-step annealing treatment. Because of the improved crystallinity and lattice orientation with two-step annealing condition, the recombination rate for the devices with two-step annealing treatment is much lower than that the devices with one-step annealing treatment.

4. CONCLUSIONS

In conclusion, we described effectively one step deposition, two-step solvent-assisted annealing method to controlling $CH_3NH_3PbI_{3-x}Cl_x$ perovskite film morphology and crystallinity, which can effectively enhance the film quality. The SEM and XRD characterizations exhibited high uniformity, large grain size and high preferred growth orientation along the [110] direction. The defect density of $CH_3NH_3PbI_{3-x}Cl_x$ film was effectively reduced, suppressing the nonradiative recombination channels. This resulted in significantly performance

DOI: 10.1021/acsami.5b03324
ACS Appl. Mater. Interfaces 2015, 7, 16330–16337

enhancement of the photovoltaic devices. Up to 14% of PCE has been achieved in FTO/bl-TiO_2/mp-TiO_2/$CH_3NH_3PbI_{3-x}Cl_x$/spiro-MeOTAD/Au perovskite devices. The two-step solvent-assisted annealing strategy offered a simple and effective method to realize high quality perovskite film for efficient hybrid perovskite solar cells.

■ ASSOCIATED CONTENT

Supporting Information

SEM images of the perovskite film obtained solution deposition method with mole ratio of PbI_2 and CH_3NH_3I at 1:1, the two-step annealed $CH_3NH_3PbI_{3-x}Cl_x$ perovskite film with second step thermal annealing time of 60 min, photocurrent density–voltage characteristics of the perovskite devices with long time solvent annealing methods, and hysteresis behavior in current–voltage curves. The Supporting Information is available free of charge on the ACS Publications website at DOI: 10.1021/acsami.5b03324.

■ AUTHOR INFORMATION

Corresponding Authors

*Tel/Fax: +86 (0)28 85412542. E-mail: wulily77@163.com
*E-mail: zhangjq@scu.edu.cn.

Notes

The authors declare no competing financial interest.

■ ACKNOWLEDGMENTS

This work was partially supported by National High Technology Research and Development Program of China (863 Program, No. 2011AA050515), the Innovation Program of Sichuan University (No. 201410610179). We are grateful to the State Key Laboratory of Oral Diseases of Sichuan University for providing SEM measurement.

■ REFERENCES

(1) Green, M. A.; Ho-Baillie, A.; Snaith, H. J. The Emergence of Perovskite Solar Cells. *Nat. Photonics* **2014**, *8*, 506–514.
(2) Lin, Q.; Armin, A.; Nagiri, R. C. R.; Burn, P. L.; Meredith, P. Electro-Optics of Perovskite Solar Cells. *Nat. Photonics* **2015**, *9*, 106–112.
(3) Burschka, J.; Pellet, N.; Moon, S.-J.; Humphry-Baker, R.; Gao, P.; Nazeeruddin, M. K.; Gratzel, M. Sequential Deposition as a Route to High-Performance Perovskite-Sensitized Solar Cells. *Nature* **2013**, *499*, 316–319.
(4) Yuan, W.; Zhao, H.; Hu, H.; Wang, S.; Baker, G. L. Synthesis and Characterization of the Hole-Conducting Silica/Polymer Nanocomposites and Application in Solid-State Dye-Sensitized Solar Cell. *ACS Appl. Mater. Interfaces* **2013**, *5*, 4155–4161.
(5) Lee, M. M.; Teuscher, J.; Miyasaka, T.; Murakami, T. N.; Snaith, H. J. Efficient Hybrid Solar Cells Based on Meso-Superstructured Organometal Halide Perovskites. *Science* **2012**, *338*, 643–647.
(6) Zhou, H.; Chen, Q.; Li, G.; Luo, S.; Song, T.-b.; Duan, H.-S.; Hong, Z.; You, J.; Liu, Y.; Yang, Y. Interface Engineering of Highly Efficient Perovskite Solar Cells. *Science* **2014**, *345*, 542–546.
(7) Jeon, N. J.; Noh, J. H.; Yang, W. S.; Kim, Y. C.; Ryu, S.; Seo, J.; Seok, S. I. Compositional Engineering of Perovskite Materials for High-Performance Solar Cells. *Nature* **2015**, *517*, 476–480.
(8) Kazim, S.; Nazeeruddin, M. K.; Gratzel, M.; Ahmad, S. Perovskite as Light Harvester: A Game Changer in Photovoltaics. *Angew. Chem., Int. Ed.* **2014**, *53*, 2812–2824.
(9) Jung, H. S.; Park, N.-G. Perovskite Solar Cells: From Materials to Devices. *Small* **2015**, *11*, 10–25.
(10) Liu, M.; Johnston, M. B.; Snaith, H. J. Efficient Planar Heterojunction Perovskite Solar Cells by Vapour Deposition. *Nature* **2013**, *501*, 395–398.
(11) Xiao, M. D.; Huang, F. Z.; Huang, W. C.; Dkhissi, Y.; Zhu, Y.; Etheridge, J.; Gray-Weale, A.; Bach, U.; Cheng, Y. B.; Spiccia, L. A Fast Deposition-Crystallization Procedure for Highly Efficient Lead Iodide Perovskite Thin-Film Solar Cells. *Angew. Chem., Int. Ed.* **2014**, *53*, 9898–9903.
(12) Xu, Y.; Zhu, L.; Shi, J.; Lv, S.; Xu, X.; Xiao, J.; Dong, J.; Wu, H.; Luo, Y.; Li, D.; Meng, Q. Efficient Hybrid Mesoscopic Solar Cells with Morphology-Controlled $CH_3NH_3PbI_{3-x}Cl_x$ Derived from Two-Step Spin Coating Method. *ACS Appl. Mater. Interfaces* **2015**, *7*, 2242–2248.
(13) Bi, D.; El-Zohry, A. M.; Hagfeldt, A.; Boschloo, G. Improved Morphology Control Using a Modified Two-Step Method for Efficient Perovskite Solar Cells. *ACS Appl. Mater. Interfaces* **2014**, *6*, 18751–18757.
(14) Dualeh, A.; Tetreault, N.; Moehl, T.; Gao, P.; Nazeeruddin, M. K.; Graetzel, M. Effect of Annealing Temperature on Film Morphology of Organic-Inorganic Hybrid Pervoskite Solid-State Solar Cells. *Adv. Funct. Mater.* **2014**, *24*, 3250–3258.
(15) Li, Y.; Cooper, J. K.; Buonsanti, R.; Giannini, C.; Liu, Y.; Toma, F. M.; Sharp, I. D. Fabrication of Planar Heterojunction Perovskite Solar Cells by Controlled Low-Pressure Vapor Annealing. *J. Phys. Chem. Lett.* **2015**, *6*, 493–499.
(16) Zhao, Y.; Zhu, K. Solution Chemistry Engineering toward High-Efficiency Perovskite Solar Cells. *J. Phys. Chem. Lett.* **2014**, *5*, 4175–4186.
(17) Conings, B.; Baeten, L.; De Dobbelaere, C.; D'Haen, J.; Manca, J.; Boyen, H.-G. Perovskite-Based Hybrid Solar Cells Exceeding 10% Efficiency with High Reproducibility Using a Thin Film Sandwich Approach. *Adv. Mater.* **2014**, *26*, 2041–2046.
(18) Xie, F. X.; Zhang, D.; Su, H.; Ren, X.; Wong, K. S.; Gratzel, M.; Choy, W. C. H. Vacuum-Assisted Thermal Annealing of $CH_3NH_3PbI_3$ for Highly Stable and Efficient Perovskite Solar Cells. *ACS Nano* **2015**, *9*, 639–646.
(19) Hsu, H. L.; Chen, C. P.; Chang, J. Y.; Yu, Y. Y.; Shen, Y. K. Two-Step Thermal Annealing Improves the Morphology of Spin-Coated Films for Highly Efficient Perovskite Hybrid Photovoltaics. *Nanoscale* **2014**, *6*, 10281–10288.
(20) Zhao, Y.; Zhu, K. CH_3NH_3Cl-Assisted One-Step Solution Growth of $CH_3NH_3PbI_3$: Structure, Charge-Carrier Dynamics, and Photovoltaic Properties of Perovskite Solar Cells. *J. Phys. Chem. C* **2014**, *118*, 9412–9418.
(21) Li, Y.; Cooper, J. K.; Buonsanti, R.; Giannini, C.; Liu, Y.; Toma, F. M.; Sharp, I. D. Fabrication of Planar Heterojunction Perovskite Solar Cells by Controlled Low-Pressure Vapor Annealing. *J. Phys. Chem. Lett.* **2015**, *6*, 493–499.
(22) Liang, P.-W.; Liao, C.-Y.; Chueh, C.-C.; Zuo, F.; Williams, S. T.; Xin, X.-K.; Lin, J.; Jen, A. K. Y. Additive Enhanced Crystallization of Solution-Processed Perovskite for Highly Efficient Planar-Heterojunction Solar Cells. *Adv. Mater.* **2014**, *26*, 3748–3754.
(23) Song, X.; Wang, W.; Sun, P.; Ma, W.; Chen, Z.-K. Additive to Regulate the Perovskite Crystal Film Growth in Planar Heterojunction Solar Cells. *Appl. Phys. Lett.* **2015**, *106*, 033901–033905.
(24) Ding, Y.; Yao, X.; Zhang, X.; Wei, C.; Zhao, Y. Surfactant Enhanced Surface Coverage of $CH_3NH_3PbI_{3-x}Cl_x$ Perovskite for Highly Efficient Mesoscopic Solar Cells. *J. Power Sources* **2014**, *272*, 351–355.
(25) Hao, F.; Stoumpos, C. C.; Liu, Z.; Chang, R. P.; Kanatzidis, M. G. Controllable Perovskite Crystallization at a Gas-Solid Interface for Hole Conductor-Free Solar Cells with Steady Power Conversion Efficiency over 10%. *J. Am. Chem. Soc.* **2014**, *136*, 16411–16419.
(26) Shi, D.; Adinolfi, V.; Comin, R.; Yuan, M.; Alarousu, E.; Buin, A.; Chen, Y.; Hoogland, S.; Rothenberger, A.; Katsiev, K.; Losovyj, Y.; Zhang, X.; Dowben, P. A.; Mohammed, O. F.; Sargent, E. H.; Bakr, O. M. Low Trap-State Density and Long Carrier Diffusion in Organolead Trihalide Perovskite Single Crystals. *Science* **2015**, *347*, 519–522.
(27) Nie, W.; Tsai, H.; Asadpour, R.; Blancon, J.-C.; Neukirch, A. J.; Gupta, G.; Crochet, J. J.; Chhowalla, M.; Tretiak, S.; Alam, M. A.; Wang, H.-L.; Mohite, A. D. High-Efficiency Solution-Processed

Perovskite Solar Cells with Millimeter-Scale Grains. *Science* **2015**, *347*, 522−525.
(28) Im, J. H.; Jang, I. H.; Pellet, N.; Gratzel, M.; Park, N. G. Growth of $CH_3NH_3PbI_3$ Cuboids with Controlled Size for High-Efficiency Perovskite Solar Cells. *Nat. Nanotechnol.* **2014**, *9*, 927−932.
(29) Wang, D.; Liu, Z.; Zhou, Z.; Zhu, H.; Zhou, Y.; Huang, C.; Wang, Z.; Xu, H.; Jin, Y.; Fan, B.; Pang, S.; Cui, G. Reproducible One-Step Fabrication of Compact $MAPbI_{3-x}Cl_x$ Thin Films Derived from Mixed-Lead-Halide Precursors. *Chem. Mater.* **2014**, *26*, 7145−7150.
(30) Xiao, Z.; Dong, Q.; Bi, C.; Shao, Y.; Yuan, Y.; Huang, J. Solvent Annealing of Perovskite-Induced Crystal Growth for Photovoltaic-Device Efficiency Enhancement. *Adv. Mater.* **2014**, *26*, 6503−6509.
(31) Stranks, S. D.; Eperon, G. E.; Grancini, G.; Menelaou, C.; Alcocer, M. J. P.; Leijtens, T.; Herz, L. M.; Petrozza, A.; Snaith, H. J. Electron-Hole Diffusion Lengths Exceeding 1 Micrometer in an Organometal Trihalide Perovskite Absorber. *Science* **2013**, *342*, 341−344.
(32) You, J.; Hong, Z.; Yang, Y.; Chen, Q.; Cai, M.; Song, T.-B.; Chen, C.-C.; Lu, S.; Liu, Y.; Zhou, H.; Yang, Y. Low-Temperature Solution-Processed Perovskite Solar Cells with High Efficiency and Flexibility. *ACS Nano* **2014**, *8*, 1674−1680.
(33) Eperon, G. E.; Burlakov, V. M.; Docampo, P.; Goriely, A.; Snaith, H. J. Morphological Control for High Performance, Solution-Processed Planar Heterojunction Perovskite Solar Cells. *Adv. Funct. Mater.* **2014**, *24*, 151−157.
(34) Kim, H.-S.; Park, N.-G. Parameters Affecting I−V Hysteresis of $CH_3NH_3PbI_3$ Perovskite Solar Cells: Effects of Perovskite Crystal Size and Mesoporous TiO_2 Layer. *J. Phys. Chem. Lett.* **2014**, *5*, 2927−2934.
(35) Zhu, W.; Yu, T.; Li, F.; Bao, C.; Gao, H.; Yi, Y.; Yang, J.; Fu, G.; Zhou, X.; Zou, Z. A Facile, Solvent Vapor-Fumigation-Induced, Self-Repair Recrystallization of $CH_3NH_3PbI_3$ Films for High-Performance Perovskite Solar Cells. *Nanoscale* **2015**, *7*, 5427−5434.
(36) Dualeh, A.; Moehl, T.; Tetreault, N.; Teuscher, J.; Gao, P.; Nazeeruddin, M. K.; Graetzel, M. Impedance Spectroscopic Analysis of Lead Iodide Perovskite-Sensitized Solid-State Solar Cells. *ACS Nano* **2014**, *8*, 362−373.

DOI: 10.1021/acsami.5b03324
ACS Appl. Mater. Interfaces 2015, 7, 16330−16337